RZ 3966 (# ZUR1807-034) 07/018/2018
Materials Science 31 pages

Research Report

Dopant-induced modifications of $Ga_xIn_{(1-x)}P$ nanowire-based p-n junctions monolithically integrated on Si (111)

Nicolas Bologna[1,2], Stephan Wirths[2], Luca Francaviglia[3], Marco Campanini[1], Heinz Schmid[2], Vasileios Theofylaktopoulos[2], Kirsten E. Moselund[2], Anna Fontcuberta i Morral[3,4], Rolf Erni[1], Heike Riel[2], Marta D. Rossell[1,2]

[1]Electron Microscopy Center, Empa, Swiss Federal Laboratories for Materials Science and Technology, Dübendorf 8600, Switzerland

[2]IBM Research-Zurich, Rüschlikon 8803, Switzerland

[3]Laboratory of Semiconductor Materials, Institute of Materials, École Polytechnique Fédérale de Lausanne, Lausanne 1015, Switzerland

[4]Institute of Physics, École Polytechnique Fédérale de Lausanne, Lausanne 1015, Switzerland

© 2018 ACS
This document is the Accepted Manuscript version of a Published Work that appeared in final form in *ACS Applied Materials and Interfaces*, copyright © American Chemical Society after peer review and technical editing by the publisher.
To access the final edited and published work see https://pubs.acs.org/doi/10.1021/acsami.8b10770

LIMITED DISTRIBUTION NOTICE

This report has been submitted for publication outside of IBM and will probably be copyrighted if accepted for publication. It has been issued as a Research Report for early dissemination of its contents. In view of the transfer of copyright to the outside publisher, its distribution outside of IBM prior to publication should be limited to peer communications and specific requests. After outside publication, requests should be filled only by reprints or legally obtained copies (e.g., payment of royalties). Some reports are available at http://domino.watson.ibm.com/library/Cyberdig.nsf/home.

Research
Africa • Almaden • Austin • Australia • Brazil • China • Haifa • India • Ireland • Tokyo • Watson • Zurich

Dopant-induced modifications of $Ga_xIn_{(1-x)}P$ nanowire-based p-n junctions monolithically integrated on Si (111)

Nicolas Bologna[1,2], Stephan Wirths[2], Luca Francaviglia[3], Marco Campanini[1], Heinz Schmid[2], Vasileios Theofylaktopoulos[2], Kirsten E. Moselund[2], Anna Fontcuberta i Morral[3,4], Rolf Erni[1], Heike Riel[2], Marta D. Rossell[1,2]*

[1]Electron Microscopy Center, Empa, Swiss Federal Laboratories for Materials Science and Technology, Dübendorf 8600, Switzerland

[2]IBM Research-Zurich, Rüschlikon 8803, Switzerland

[3]Laboratory of Semiconductor Materials, Institute of Materials, École Polytechnique Fédérale de Lausanne, Lausanne 1015, Switzerland

[4]Institute of Physics, École Polytechnique Fédérale de Lausanne, Lausanne 1015, Switzerland

ABSTRACT: Today, silicon is the most used material in photovoltaics, with a maximum conversion efficiency getting very close to the Shockley-Queisser limit for single-junction devices. Integrating silicon with higher bandgap ternary III-V absorbers is the path to increase the conversion efficiency. Here, we report on the first monolithic integration of $Ga_xIn_{(1-x)}P$ vertical

nanowires, and the associated p-n junctions, on silicon by the Au-free template-assisted selective epitaxy (TASE) method. We demonstrate that TASE allows for a high chemical homogeneity of ternary alloys through the nanowires. We then show the influence of doping on the chemical composition and crystal phase, the latter previously attributed to the role of the contact angle in the liquid phase in the vapor-liquid-solid technique. Finally, the emission of the p-n junction is investigated, revealing a shift in the energy of the intra-band levels due to the incorporation of dopants. These results clarify some open questions on the effects of doping on ternary III-V nanowire growth and provide the path towards their integration on the silicon platform in order to apply them in next-generation photovoltaic and optoelectronic devices.

KEYWORDS: semiconductor nanowires, $Ga_xIn_{(1-x)}P$, template-assisted selective epitaxy, scanning transmission electron microscopy, doping, cathodoluminescence, solar cells

INTRODUCTION: Crystalline silicon photovoltaic (PV) solar cells constitute one of the world's leading source of renewable energy generation[1] with a maximum power efficiency of 26.7% [2]. This value, which is very close to the theoretical limit of 29.4 % [3], certainly constitutes the first step for the establishment of PV technologies as a valid competitor over fossil fuels in the long term. In the last decade, multi-junction solar cells made of III-V semiconductors have been developed as valid alternative devices able to push the efficiency up to 46% by absorbing different wavelengths of the solar spectrum under concentrated sunlight illumination [4]. III-V triple-junction thin films monolithically integrated on a standard Si wafer have also been demonstrated recently with an efficiency of 33.3% [5]. In order to increase the efficiency of multi-junction solar cell devices, III-V nanowires (NWs) monolithically integrated on silicon substrate

could be employed [6–8]. NWs are high aspect ratio crystalline structures that, when implemented on a Si platform, would allow to significantly reduce III-V material usage and the associated cost and at the same time ensure an extremely high absorption of light thanks to the optimal coupling [9–16]. Additionally, the small interface area of the NWs is very effective at minimizing stresses commonly arising during the epitaxial growth of lattice and thermal mismatched thin films. Thus, the efficient strain relaxation in thin nanowires allows extending the possible material combinations needed to grow NW heterostructures [17–22].

$Ga_xIn_{(1-x)}P$ NWs are currently attracting great interest as a promising nanostructured material system for efficient photovoltaic solar cells [23,24]. Due to their direct and tunable bandgap over a wide range of compositions (1.35-2.26 eV), $Ga_xIn_{(1-x)}P$ NWs, integrated on a Si substrate (1.12 eV), can be designed to absorb light from the major part of the visible solar spectrum [25–27]. Thus, by intentionally varying the composition, the dopant type and concentration along the NWs, different parts of the spectrum can be absorbed and loss of energy through carrier thermalization minimized. These properties have important economic implications to meet the demand for both high efficiency and low-cost solar cells. Still, in order to successfully integrate III-V NWs on Si in a tandem (multi-junction) geometry, two critical aspects are here addressed: i) the demonstration of composition controlled high-quality $Ga_xIn_{(1-x)}P$ nanowires on Si substrates and ii) the effect of doping on the NW composition, microstructure and morphology.

To the best of our knowledge, catalyst-free and high-quality growth of doped $Ga_xIn_{(1-x)}P$ NWs on (111)-oriented Si substrates have not been achieved, mainly due to the compositional inhomogeneities occurring during dopant incorporation [28–32]. In addition, it is widely reported that the use of dopants during nanowire growth, apart from modifying the chemical composition, can also affect in some cases the morphology (i.e. NW diameter) and the crystal structure (e.g.

crystal polytypism). For example, Zn doping modifies the wetting angle of the metallic seed particle during the NW growth favoring the zinc-blende crystal structure in InP and $Ga_xIn_{(1-x)}P$ NWs [33,34]. On the contrary, the addition of Zn and Sn dopants in GaAs NWs causes either an increase in the wurtzite proportion or no effect at all [35–37]. Moreover, the presence of Au as catalyst in VLS might compromise the Si PV cell performance. First attempts to grow $Ga_xIn_{(1-x)}P$ NWs without the use of any catalyst particle were realized by selective-area epitaxy (SAE) with good control of the NW morphology and composition [27,38], but this work relied on the use of InP substrates.

The template-assisted selective epitaxy technique (TASE) allows for the growth of shape- and size-controlled nanostructures by means of a silicon oxide nanotube template offering a wide growth parameter window (as compared to SAE) and well-defined growth direction [39–42]. These characteristics render the TASE technique attractive to obtain NW structures on Si for solar cell applications.

In the present work, we demonstrate the first successful monolithic integration of $Ga_xIn_{1-x}P$ nanowires on (111)-oriented Si substrates using TASE. Furthermore, we present a comparative study between intrinsic and doped $Ga_xIn_{(1-x)}P$ NWs including p-n junctions using aberration-corrected high-angle annular dark-field scanning transmission electron microscopy (HAADF-STEM) in combination with energy dispersive x-ray spectroscopy (EDX) and electron energy-loss spectroscopy (EELS). Thus, the effect of doping on the microstructure and composition of the NWs is revealed. Finally, the optical properties of individual doped NWs are probed by cathodoluminescence (CL) spectroscopy.

RESULTS AND DISCUSSION: An overview scanning electron microscopy (SEM) image of an array of TASE-grown vertical $Ga_xIn_{(1-x)}P$ NWs on a Si(111) substrate is displayed in Figure

1. The right panel shows a magnified image of a single $Ga_xIn_{(1-x)}P$ NW grown onto the Si seed crystal into the predefined SiO_2 nanotube template. Site-specific TEM lamellae for STEM characterization were prepared by using a focused ion beam (FIB) instrument.

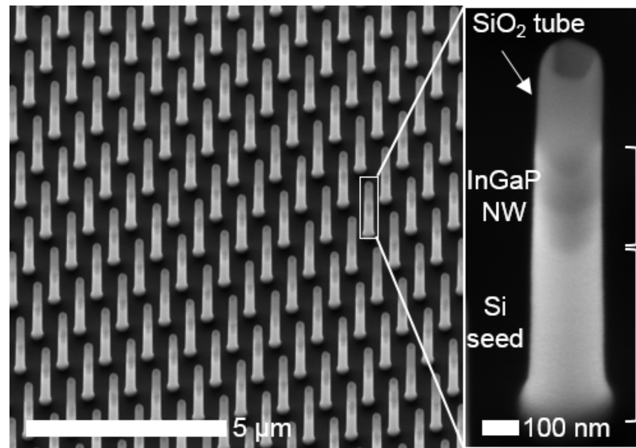

Figure 1. Tilted view SEM micrograph of a highly ordered $Ga_xIn_{(1-x)}P$ NW array grown on a Si(111) substrate. A magnified view of a single NW is shown in the right panel. The SiO_2 nanotube template (partially empty), the Si seed and the $Ga_xIn_{(1-x)}P$ NW are indicated.

A typical undoped NW is shown along the $[\bar{1}10]$ zone axis in the STEM micrograph of Figure 2a. On average, these NWs possess a diameter of about 150 nm with a flat front facet and a sharp interface with the Si substrate. Concerning the crystal structure, the zinc-blende type dominates the entire length of the NW with a high density of planar defects (stacking faults and twins) lying on the $(\bar{1}\bar{1}\bar{1})$ plane. This is clearly visible in the atomic-resolution images of Figures 2b and 2c obtained at the top (red window in Figure 2a) and at the bottom (blue window in Figure 2a) of the NW, respectively. No difference in the type of planar defects has been observed between the two regions. A detailed analysis of the interface with the silicon seed was performed

by geometric phase analysis (GPA) in order to detect possible defect formation due to the lattice mismatch. Figure 2d shows a magnified view of the green squared region highlighted in Figure 2a. The corresponding ε_{yy} strain map along the out-of-plane direction is displayed in Figure 2e. Here, the $Ga_xIn_{(1-x)}P$ NW appears to have a positive deformation (red colour) as the lattice parameter is larger than the Si used as reference, which is a_{Si} = 5.431 Å. The value for the strain measured at the $Ga_xIn_{(1-x)}P$ area is 6.5 ± 0.3 % resulting in a lattice constant of 5.78 ± 0.1 Å. Three blue arrows in the HAADF image indicate the regions of the interface exhibiting a lower contrast due to an interruption of the atomic stacking continuity. In the strain map of Figure 2e, these regions are clearly recognizable by the three compressive-tensile butterfly-like strain features separated by an average distance of about 4.5 nm. They are interfacial misfit dislocations which form to release the mismatch strain between both systems [43]. The compositional homogeneity of the undoped nanowires was then investigated by STEM-EDX. For this analysis, the NWs were transferred to a holey carbon-coated TEM copper grid by gently rubbing it against the NW array. Thus, gallium contamination due to the FIB sample preparation was avoided. A HAADF-STEM image of a typical undoped nanowire and the corresponding elemental maps calculated from a EDX spectrum image using the P-Kα_1, In-Lα_1, and Ga-Kα_1 lines are shown in Figures 2f-i. As revealed in Figure 2h and 2i, the composition of the undoped NWs is fairly homogeneous both in the longitudinal and radial directions with In, Ga, and P nearly constant across the entire structure with a few regions showing slight variations in the Ga/In content. The compositional line-profiles obtained by averaging the integrated intensities over the whole diameter of the NW are given in Figure 2j. While small oscillations are perceptible in the indium and gallium line profiles (most likely due to variations in the growth rate of {111}- and {110}-type facets during the growth process), an average $Ga_xIn_{(1-x)}P$

composition with $x = 0.25 \pm 0.03$ can be obtained for the undoped NWs. This corresponds to a lattice constant of 5.77 ± 0.02 Å, leading to a lattice mismatch of 6.1 ± 0.4 % with silicon.

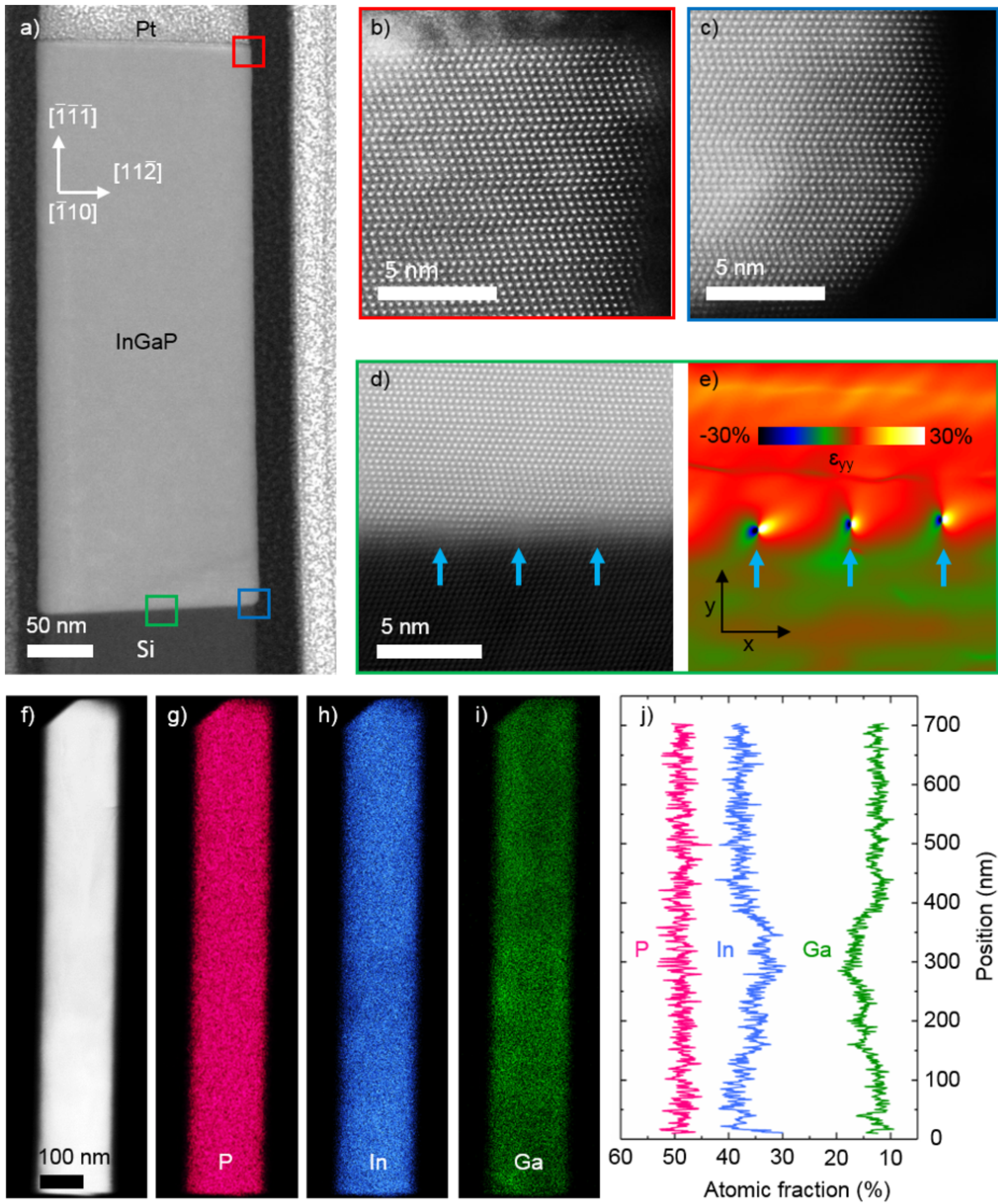

Figure 2. (a) HAADF-STEM overview image showing a typical undoped $Ga_xIn_{(1-x)}P$ NW. Atomic resolution HAADF-STEM detail of the crystal structure at the top (b, red) and at the bottom (c, blue) of the NW. Both areas exhibit a zinc-blende crystal structure with a high-density of planar defects. (d) Magnified image of a region at the $Ga_xIn_{(1-x)}P$/Si interface corresponding to the green square. Three misfit dislocations are marked with blue arrows and appear in panel (e) as butterfly-like features in the out-of-plane (ε_{yy}) strain map obtained by GPA. (f) HAADF-STEM image of an undoped NW and corresponding elemental maps of (g) phosphorous, (h) indium and (i) gallium obtained from an EDX spectrum image. (j) Compositional line profiles of P, In and Ga obtained by averaging the integrated intensities over the whole diameter of the NW.

Similarly, p-n homojunction NWs were also characterized by employing HAADF-STEM and STEM-EDX. Figure 3a shows an overview image of a representative doped NW exhibiting a sharp interface with the Si substrate, comparable to the undoped structures. For this particular NW, the front facet is not regular, probably due to the milling process during the FIB preparation, and therefore no particular faceting can be recognized. For the doped NWs two features are readily observed: the first one, indicated with a yellow arrow in Figure 3a, is a sharp change of contrast along the growth direction arising at about 260 nm from the silicon interface, which can be associated with the switch from the n- to the p-region of the nanowire combined with a change in composition as it will be discussed below. The second feature is highlighted with two white arrows in the upper left area of Figure 3a. Two dark stripes propagate from the top of the NW to the left sidewall. The atomically-resolved HAADF-STEM image of Figure 3c (obtained from the blue squared region in Figure 3a), unveils a zinc-blende structure with a high density of twins (about 1 twin/nm) lying on the $(\bar{1}\bar{1}\bar{1})$ plane, similarly to the undoped structure.

This morphology is observed from the interface with the silicon until the previously mentioned change in contrast at 260 nm. Then, the upper half of the NW presents also a zinc-blende structure, but with a much lower density of planar defects (5 twins in the entire upper segment) lying on parallel $(1\bar{1}1)$ planes. These twins are visible as darker stripes in the overview image of Figure 3a (white arrows) and are highlighted with red dashed lines in the atomically resolved HAADF-STEM image of Figure 3b which corresponds to the red area in panel a. This change in crystal structure from the bottom to the top of the NW is related to the transition from the n-doped (Si) to the p-doped (Zn) segment. A preferential growth of the zinc-blende crystal structure was previously attributed to a variation in the wetting angle of the gold seed particle caused by the introduction of Zn dopant atoms in NWs grown by VLS[34]. Likewise, changes in the NW diameter were attributed to the seed particle wetting angle. However, our results demonstrate that a change in the crystal structure also occurs when no metal catalyst particle is used for the NW growth. Additionally, as the TASE method employs nanotube templates for the growth of the NWs the diameter of neither doped nor undoped structures is altered by the introduction of dopants, maintaining the original aspect ratio necessary for high-performance solar cells. Additionally, our observations unveil that the addition of dopant atoms in the NWs affects the density of misfit dislocations at the $Ga_xIn_{(1-x)}P$/Si interface. In the HAADF-STEM image and the corresponding ε_{yy} strain map of Figures 3d and 3e, respectively, it can be seen that the distance between misfit dislocations is here increased to about 5.5 nm while the experimentally measured strain difference between the NW and the Si substrate is only ~4.5 ± 0.3 %. This value corresponds to a lattice constant of 5.68 ± 0.1 Å, that is smaller than in the undoped structure. To confirm these results and to unveil the origin of the sharp contrast change observed at the middle of the doped NWs, we acquired EDX spectrum images of several wires.

Similarly to the undoped NWs, the sample for EDX analysis was prepared by gently rubbing the TEM grid against the chip's surface. A representative doped NW is shown in Figure 3f, while the elemental maps calculated from the EDX spectrum image (P-Kα_1, In-Lα_1, and Ga-Kα_1 lines) are presented in Figures 3g-i. It is evident that the bottom part of the NW contains a higher amount of indium while the top segment is gallium rich. This effect was further studied on six different doped NWs by recording the amount of indium, gallium, and phosphorus in three different positions along the structures, i.e. at 50, 150 and 500 nm from the Si seed. The obtained results are shown in Figure 3j where each data point corresponds to the average value of 6 wires and the error bars are given by the calculated standard deviation ($\pm 1\sigma$). While the phosphorus is constant along the whole length of all six NWs, the indium and gallium profiles show a drastic change from the bottom to the top of the NW. The region close to the silicon seed has an average $Ga_xIn_{(1-x)}P$ composition with $x = 0.33 \pm 0.05$, i.e. a lattice constant of 5.73 ± 0.03 Å. This experimental value is, as expected, smaller than the one observed for the undoped NW (5.85 Å), explaining the larger dislocation spacing. Instead, at the upper segment, the trend is reversed and we find a maximum Ga content with an average $x = 0.55 \pm 0.03$, corresponding to a lattice constant of 5.64 ± 0.01 Å. The change in composition takes place within ~40 nm at the p-n interface (see Figure S1 in the Supporting Information) and results in a lattice mismatch of -1.6%. However, no structural defects are detected at any of the investigated p-n junctions (see Figure S2 in the Supporting Information). Finally, although the change from n to p doping is typically observed at about 150 nm from the silicon interface (coinciding with a similar concentration of Ga and In), p-n junctions are occasionally detected at a longer distance from the Si interface (as in the NW displayed in Figure 3a) due to different growth rates of the n-segments.

Our observations concerning the influence of doping on the chemical composition of p-doped $Ga_xIn_{(1-x)}P$ nanowires are in agreement with previous works stating that DEZn increases the incorporation of Ga due to the enhanced pyrolysis of the TMGa related species [34,44]. Furthermore, our results provide the first experimental evidence that Si doping also boosts the incorporation of Ga in the n-doped section, as compared to the undoped structure, while a high density of stacking faults perpendicular to the growth direction is still present.

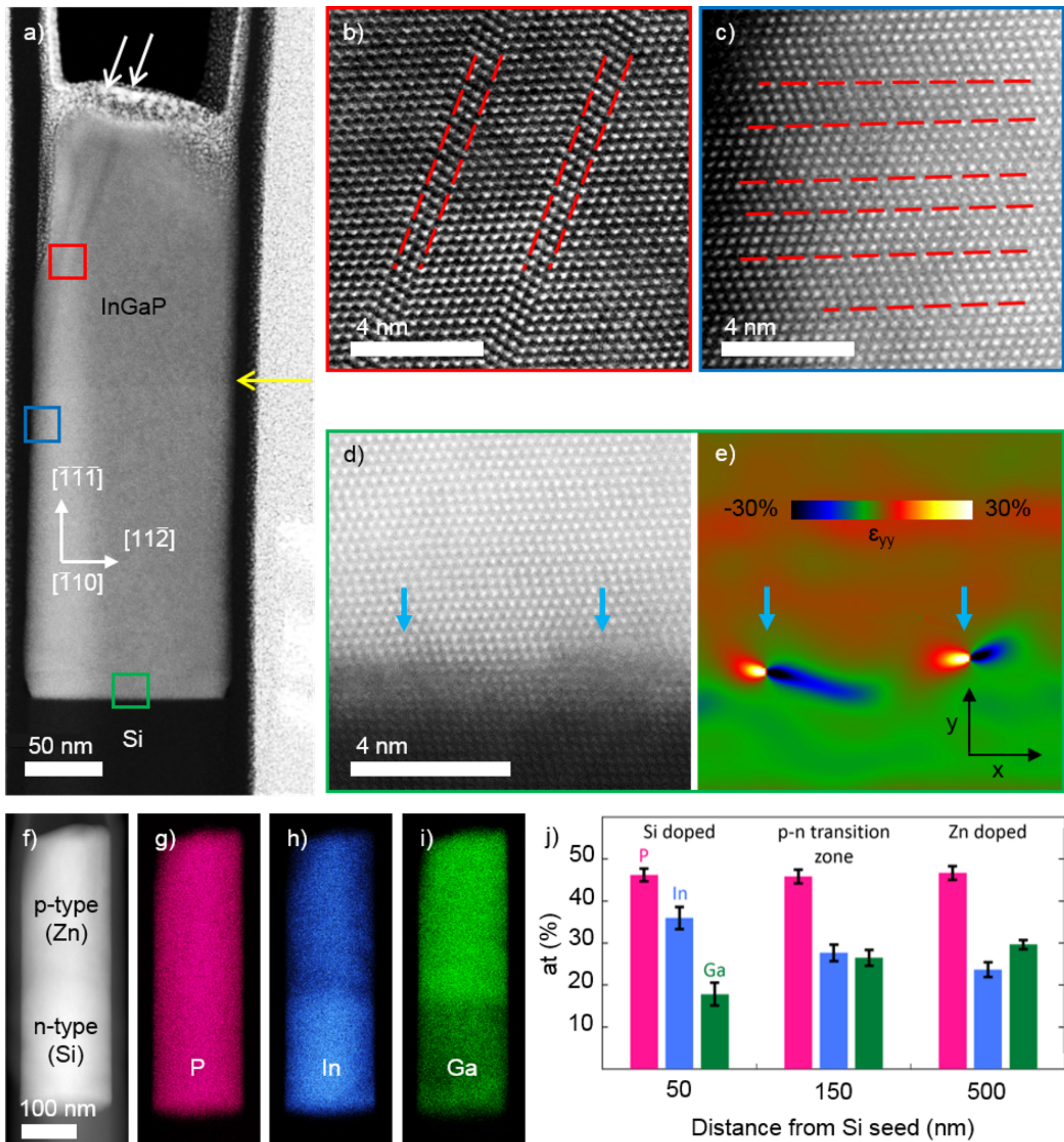

Figure 3. (a) HAADF-STEM overview image showing a representative p-n doped $Ga_xIn_{(1-x)}P$ NW. Atomic resolution HAADF-STEM detail of the crystal structure of the top (b, red) and at the bottom segment (c, blue) of the NW. A yellow arrow indicates the transition from the top p-doped (Zn) segment and the bottom n-doped (Si) section exhibiting a high density of planar defects (highlighted by red dashed lines). (d) Magnified image of a region at the $Ga_xIn_{(1-x)}P$/Si

interface corresponding to the green square. Two misfit dislocations are marked with blue arrows and appear in panel (e) as butterfly-like features in the out-of-plane (ε_{yy}) strain map obtained by GPA. (f) HAADF-STEM image of a p-n doped $Ga_xIn_{(1-x)}P$ NW and corresponding elemental maps of (g) phosphorus, (h) gallium and (i) indium obtained from an EDX spectrum image. (j) Bar chart showing the In, Ga, and P content at three different positions (50, 150 and 500 nm from the Si seed) averaged for six different NWs. The P content (pink) is constant in all NWs, while the In (light blue) and Ga (green) profiles display a reverse trend with a comparable composition at about 150 nm.

The incorporation of dopants is expected to also modify the overall electron density in the doped NWs since the resulting number of valence electrons is different from that of the undoped material. Here, EELS was applied to determine changes of the valence electron density across the NWs. In particular, in the low-loss region of the EELS spectrum, the most prominent feature corresponds to plasmon losses. Plasmon losses are collective oscillations of the valence electrons and their energy is related to the density of the valence electrons. Therefore, changes in the valence electron density will be reflected by changes in the plasmon energy peak [45]. The doped NW displayed in Figure 4a is the same as the one investigated by EDX in Figure 3f. The green rectangle indicates the area in which the EELS spectrum was acquired. After aligning the spectrum image by using the zero-loss peak, the spectra were background subtracted by fitting a decaying power-law function to an energy window just in front of the plasmon peaks. Thus, two distinct plasmon peaks were obtained for the n- and p-doped sections of the NW at a plasmon energy $E_{p,n} = 15.0\ eV$ and $E_{p,p} = 15.6\ eV$, respectively (see Figure 4c). The same analysis performed on six different NWs gave average plasmon energy values of 15.0 ± 0.09 eV and

15.51 ± 0.07 eV for the n- and p-doped section, respectively. Figure 4b shows the plasmon energy map obtained by performing a non-linear least square fitting (NLLS) to the acquired spectrum image and corresponding to the region in the green rectangle in Figure 4a. The difference in bulk plasmon energy at the bottom and at the top of the NW is evident, demonstrating that the distinct doping incorporation affects both the chemical and the electronic properties of the material. However, from the EDX results obtained previously, we infer that this energy shift is mainly caused by a change in the Ga/In ratio across the NW rather than merely by the presence of dopant atoms. For this reason, as the bulk plasmon energy E_p varies linearly with composition[46], we used the two extreme compositions (InP and GaP) as standards to check the validity of our measurements. The reference spectra (acquired using the same experimental conditions) from bulk InP and GaP exhibit bulk plasmon peaks at $E_p = 14.37\ eV$ and $E_p = 16.55\ eV$, respectively. By performing a linear regression, we obtained the following equation for the plasmon energy in eV:

$$E_p[eV] = 0.0218x + 14.37 \tag{1}$$

where x is the gallium percentage. Thus, by using the E_p values extracted from the plasmon map, an average composition of $x = 0.29 \pm 0.04$ and $x = 0.52 \pm 0.03$ is obtained, corresponding to a lattice constant equal to 5.74 ± 0.02 Å and 5.64 ± 0.01 Å for the n- and the p-doped segment, respectively. These values are in excellent agreement with the data derived from the EDX measurements. No remarkable changes in the width of the plasmon peak (~3.0 eV) were detected between the top and the bottom of the NW. The $Ga_xIn_{(1-x)}P$ lattice parameters obtained by GPA,

STEM-EDX and STEM-EELS from the undoped and doped nanowires are summarized in Table 1.

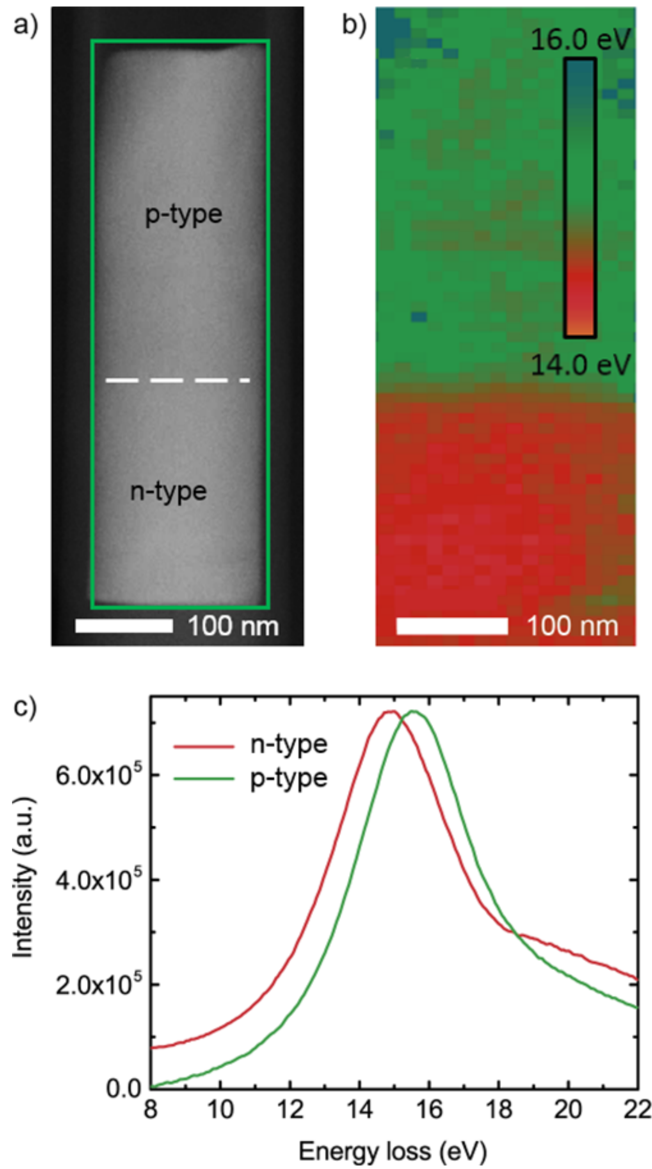

Figure 4. (a) HAADF-STEM micrograph of a p-n doped NW with overlaid green rectangle corresponding to the area used for EELS spectrum image acquisition. (b) Bulk plasmon map extracted from the EELS spectrum image evidencing the presence of two distinct regions with different plasmon energies. (c) Bulk plasmon peaks extracted from the spectrum image at the n- (green) and p-doped (red) sections.

Table 1. $Ga_xIn_{(1-x)}P$ Lattice Parameters of Undoped and Doped Nanowires Obtained by GPA, STEM-EDX and STEM-EELS.

	$Ga_xIn_{(1-x)}P$ lattice parameter (Å)		
	undoped	n-segment	p-segment
GPA	5.78 ± 0.10	5.68 ± 0.10	-
EDX	5.77 ± 0.02	5.73 ± 0.03	5.64 ± 0.01
EELS	-	5.74 ± 0.02	5.64 ± 0.01

CL measurements were carried out in order to access the optical characteristics of the p-n junction and to link them to the compositional characterization previously presented. In Fig. 5a it is shown a SEM image of a doped nanowire. The corresponding false-colored CL map is displayed in Fig. 5b: red corresponds to the emission centered at 1.73 eV, green to 1.93 eV and blue to 1.98 eV. This color coding identifies three different regions of emission along the NW long axis, which overlap with the positions of the n- and p-doped sides of the junction as well as with the transition region between these two. Figure 5c shows CL spectra representative of the three distinct areas observed in Fig. 5b. The CL data in both Fig. 5b and c show that the emission energy from the n-doped segment is lower (1.73 eV) than the one from the p-doped (1.93 eV).

The emission-energy difference between the p- and n-type regions can be mainly explained by the different alloy composition observed by EDX and EELS [47]. Yet, the experimental emission energy is lower than the expected bandgap; in particular in the p-doped segment the emission is few tens of meV lower than the low-temperature bandgap values reported in the literature [47,48]. The exciton binding energy of bulk GaInP is too small to justify this redshift [49]. On the contrary, in both the p and the n regions we estimate high concentrations of dopants (exceeding 10^{18} cm^{-3}), which can cause a narrowing of the optical bandgap and account for the observed redshift. It is also interesting to notice that the redshift is less pronounced in the n-type NW segment. Since Si is used as a dopant in this segment, this is probably a consequence of the compensation that affects the Si doping [50].

At the interface, both peaks are visible and show a blueshift with respect to those observed farther from the interface. Such a blueshift is more pronounced in the case of the emission related with the p-type segment (1.98 eV) than the one related with the n-type segment (1.74 eV). Here, the CL beam mainly probes the depletion region of the p-n junction. As a result the emission energy blueshifts and approaches the electronic-bandgap energy (2.04 eV for the p-type $Ga_{0.55}In_{0.45}As$ segment and 1.74 eV for the n-type $Ga_{0.33}In_{0.67}As$ segment [47]). Other phenomena may also contribute to the shift of the emission energy in CL. For instance, the high power density of the electron beam can blueshift the emission by bandgap filling [51] and alloy reordering is reported to redshift the GaInP emission by 100 meV [52]. However, the fact that the CL signal blueshifts at the p-n interface and redshifts elsewhere with respect to the intrinsic bandgap supports the role of the dopant levels as a mediator of the observed luminescence.

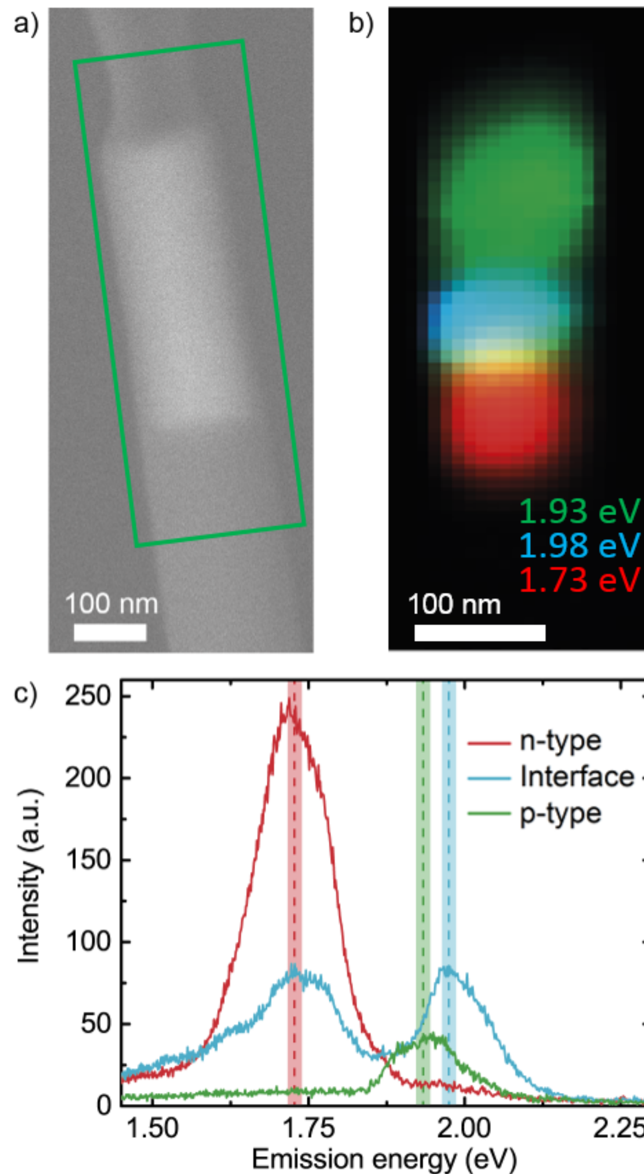

Figure 5 (a) SEM image of the doped nanowire investigated by CL. (b) False-colored CL map corresponding to the green window in panel (a) extracted from the CL spectrum image evidencing the presence of three distinct regions with different emission energies. (c) Emission bands extracted from the spectrum image at the bottom n-doped (green) segment, top p-doped (red) segment and at the interface (blue). The dashed lines highlight the emission peaks 1.73 eV (red), 1.93 eV (green) and 1.98 eV (light blue) used for the CL map.

CONCLUSIONS AND OUTLOOK: In conclusion, we have demonstrated the first monolithic integration of $Ga_xIn_{(1-x)}P$ vertical NWs on (111)-oriented Si substrates by using TASE. By employing a combination of aberration-corrected HAADF-STEM imaging and spectroscopy techniques, we have measured the structural and compositional properties of intrinsic and doped $Ga_xIn_{(1-x)}P$ NWs. We show that, in absence of dopants, TASE allows growing highly homogeneous nanowires with a zinc-blende structure and a high density of planar defects. Next, our observations show that the addition of Zn atoms as p-dopants results in a clear reduction of the number of stacking faults with a subsequent increase of the Ga incorporation, proving that the preferential growth of the zinc-blende phase is not uniquely associated with a modification of the wettability of the metal nano-catalyst, as previously reported [34,53]. Finally, by performing CL measurements we provide experimental evidence that donor and acceptor energy levels are introduced in the energy gap by the dopant atoms. The results presented here provide new insights into the integration and doping of ternary III-V nanowires on the silicon platform for the next generation of photovoltaic and optoelectronic devices.

METHODS. *Nanowire Growth.* The nanostructures were grown in nanotube templates by metal-organic chemical vapor deposition (MOCVD) on Si (111) wafers at a temperature of 550°C. The vertical templates were fabricated with the following procedure. A sacrificial amorphous α-Si layer was sputtered on the wafer's surface. The thickness of the α-Si layer determines the height of the templates, while the diameter (~150 nm) and position of the templates are defined by patterning hydrogen silsesquioxane (HSQ) dots by electron beam

lithography. Inductively-coupled plasma reactive-ion etching using HBr/O_2 was employed to etch out vertical Si nanowires. SiO_2 was then subsequently deposited on the Si nanowires by plasma enhanced chemical vapor deposition at 400 °C. In order to empty the nanotube templates and to obtain a pristine (111)-terminated crystalline Si surface at the bottom, a patterned resist mask was deposited to protect the substrate and a 25% tetramethylammonium hydroxide solution was used to selectively etch away the Si sacrificial nanowires. The growth of the $Ga_xIn_{(1-x)}P$ NWs was carried out using trimethylindium (TMIn), trimethylgallium (TMGa) and tertiarybutylphosphine (TBP) with a V/III ratio of 310. A group III molar flux ratio of (TMGa/(TMGa+TMIn) of 0.6 to 0.25 was used. The doped NWs were grown with the same conditions but with a V/III ratio of 42. The n-type doping, induced in the first half of the NWs, was obtained by using disilane (Si_2H_6) with a molar flux ratio Si/(TMIn+TMGa) of 0.0023 while for the p-type doping, induced in the second half of the NWs, diethylzinc (DEZn) was employed with a ratio DEZn/(TMIn+TMGa) of 3 resulting in doping concentrations above $1.0 \times 10^{18} cm^{-3}$ for both sections [54]. In general, the observed growth rate was about 10 nm/min for the undoped and doped samples.

Sample preparation. TEM lamellas for atomic-resolution investigations were prepared with an FEI Helios Nanolab 450S FIB instrument. In order to minimize gallium implantation by the Ga^+ ion beam, the region of interest was protected with a 100-nm-thick platinum layer deposited by electron beam induced deposition at a voltage of 5 kV and 100 pA of current. After isolating the primitive lamella with rough cuts employing a voltage of 30 kV and decreasing currents, a tungsten Omniprobe probe was used to extract and attach the section to an Omniprobe TEM copper grid. Finally, the lamella was thinned down to electron transparency (i.e. below 100 nm) with a voltage and current of the Ga^+ ion beam of 5 kV and 50 pA, respectively. For the EDX,

EELS and CL measurements, the NWs, still incorporated in the oxide templates, were transferred to a holey carbon-coated TEM copper grid by gently rubbing the it against the wires. Thus, gallium contamination due to FIB sample preparation was avoided.

TEM characterization. The morphology and microstructure of the NWs were assessed by means of a double spherical aberration-corrected JEOL JEM-ARM200F instrument operated in probe-corrected STEM mode with a convergence semiangle of 25 mrad and a spatial resolution of 80 pm at 200 kV. The collection angles for the HAADF detector were in the 90-170 mrad range.

Atomic resolution imaging and GPA within the FRWRTools plug-in[55] were used to determine the crystal structure of the NWs and to detect the presence of structural defects at the NW-substrate interface. The compositional homogeneity of the NWs was addressed by performing quantitative EDX maps by means of an FEI Titan Themis operated at 300 kV and equipped with ChemiSTEM technology. The spectra were recorded with a beam current of 0.3 nA, 0.8 nm pixel spacing and a dwell time of 10 µs per pixel. EELS plasmon mapping of doped NWs was performed with a Jeol JEM ARM-200F equipped with a Gatan Enfinium EELS spectrometer. For the EELS data acquisition, the convergence and collection semi-angles were set to 25.3 and 33 mrad, respectively. An exposure time of 0.4 s and a dispersion of 0.05 eV/channel were used in combination with a current of about 4.8 µA. For these values, the energy resolution measured at the full-width-at-half-maximum of the zero-loss peak in vacuum was 0.55 eV.

CL characterization. The CL experiment was performed with an Attolight SEM-CL microscope, operated at a temperature of 12 K. An acceleration voltage of 10 kV and a current in the order of 1 nA was used. The exposure time and the pixel size were 100 ms and 2 nm, respectively. The emitted light from the NWs was captured by a dispersive spectrometer with a

focal length of 32 cm and a grating of 150 l/mm and detected by a Peltier-cooled CCD camera, resulting in a spectral resolution of 1.6 nm.

ASSOCIATED CONTENT

The supporting information is available free of charge and provides further information about the compositional variations at the p-n interface, the atomic-resolution study at the p-n junction and the simulation performed with NextNano to study the band alignment.

AUTHOR INFORMATION

Corresponding author

*E-mail: nicolas.bologna@empa.ch

Author contributions

The manuscript was written through contributions of all authors. N.B. performed the FIB preparation, the STEM and the GPA investigation. M.C. supervised the STEM and GPA analysis. S.W. and H.S. were responsible for the growth of the NWs. N.B., L.F. and T.V. performed the CL measurements. K.M., A.F.M, R.E., H.R. and M.D.R. have supervised the project. All authors have given approval to the final version of the manuscript.

Funding Sources

This research was financially supported by the European Union H2020 program Nano-Tandem (Grant Agreement No. 641023) and the Swiss National Science Foundation (project no. 200021_156746 and 200021_169908 through the NCCR QSIT).

Notes

The authors declare no competing financial interest

ACKNOWLEDGMENTS

The authors gratefully acknowledge L. Czornomaz, P. Staudinger, C. Convertino, M. Sousa and V. Piazza for the valuable discussions.

REFERENCES

(1) REN21 Secretariat, Renewables 2017 global status report.

(2) Yoshikawa, K.; Kawasaki, H.; Yoshida, W.; Irie, T.; Konishi, K.; Nakano, K.; Uto, T.; Adachi, D.; Kanematsu, M.; Uzu, H.; Yamamoto, K. Silicon Heterojunction Solar Cell with Interdigitated Back Contacts for a Photoconversion Efficiency Over 26% Nat. Energy **2017**, 2 (17032), 1–8.

(3) Richter, A.; Hermle, M.; Glunz, S. Reassessment of the Limiting Efficiency for Crystalline Silicon Solar Cells IEEE J. Photovoltaics **2013**, 3 (4), 1184–1191.

(4) Green, M. A.; Hishikawa, Y.; Dunlop, E. D.; Levi, D. H.; Hohl-Ebinger, J.; Ho-Baillie, A. W. Y. Solar Cell Efficiency Tables (version 51) Prog. Photovoltaics Res. Appl. **2018**, 26 (1), 3–12.

(5) Cariou, R.; Benick, J.; Feldmann, F.; Höhn, O.; Hauser, H.; Beutel, P.; Razek, N.; Wimplinger, M.; Bläsi, B.; Lackner, D.; Hermle, M.; Siefer, G.; Glunz, S. W.; Bett, A. W.; Dimroth, F. III–V-on-silicon Solar Cells reaching 33% Photoconversion Efficiency in Two-terminal Configuration Nat. Energy **2018**, 3, 326-333.

(6) Kempa, T. J.; Lieber, C. M. Semiconductor Nanowire Solar Cells: Synthetic Advances and Tunable Properties Pure Appl. Chem. **2014**, 86 (1), 13–26.

(7) Tian, B.; Kempa, T. J.; Lieber, C. M. Single nanowire photovoltaics Chem. Soc. Rev. **2009**, 38 (1), 16–24.

(8) Kandala, A.; Betti, T.; I Morral, A. F. General Theoretical Considerations on Nanowire Solar Cell Designs Phys. Status Solidi Appl. Mater. Sci. **2009**, 206 (1), 173–178.

(9) Zhu, J.; Yu, Z.; Burkhard, G. F.; Hsu, C.-M.; Connor, S. T.; Xu, Y.; Wang, Q.; McGehee, M.; Fan, S.; Cui, Y. Optical Absorption Enhancement in Amorphous Silicon Nanowire and Nanocone Arrays Nano Lett. **2009**, 9 (1), 279–282.

(10) Frederiksen, R.; Tutuncuoglu, G.; Matteini, F.; Martinez, K. L.; Fontcuberta, A.; Alarcon-Llado, E. Visual Understanding of Light Absorption and Waveguiding in Standing Nanowires with 3D Fluorescence Confocal Microscopy ACS Photonics **2017**, 4 (9), 2235–2241.

(11) Krogstrup, P.; Jørgensen, H. I.; Heiss, M.; Demichel, O.; Holm, J. V.; Aagesen, M.; Nygard, J.; Fontcuberta I Morral, A. Single-nanowire Solar Cells Beyond the Shockley–Queisser Limit Nat. Photonics **2013**, 7 (4), 306–310.

(12) Diedenhofen, S. L.; Janssen, O. T. A.; Grzela, G.; Bakkers, E. P. A. M.; Gómez Rivas, J. Strong Geometrical Dependence of the Absorption of Light in Arrays of Semiconductor Nanowires ACS Nano **2011**, 5 (3), 2316–2323.

(13) Chen, Y.; Pistol, M. E.; Anttu, N. Design for Strong Absorption in a Nanowire Array Tandem Solar Cell Sci. Rep. **2016**, 6 (August), 1–8.

(14) Green, M. A.; Emery, K.; King, D. L.; Igari, S.; Warta, W. Solar Cell Efficiency Tables (Version 18) Prog. Photovoltaics Res. Appl. **2001**, 9 (4), 287–293.

(15) Tobías, I.; Luque, A. Ideal Efficiency of Monolithic, Series-Connected Multijunction Solar Cells Prog. Photovoltaics Res. Appl. **2002**, 10 (5), 323–329.

(16) Wallentin, J.; Anttu, N.; Asoli, D.; Huffman, M.; Aberg, I.; Magnusson, M. H.; Siefer, G.; Fuss-Kailuweit, P.; Dimroth, F.; Witzigmann, B.; Xu, H. Q.; Samuelson, L.; Deppert, K.; Borgstrom, M. T. InP Nanowire Array Solar Cells Achieving 13.8% Efficiency by Exceeding the Ray Optics Limit Science. **2013**, 339 (6123), 1057–1060.

(17) Kim, S. K.; Day, R. W.; Cahoon, J. F.; Kempa, T. J.; Song, K. D.; Park, H. G.; Lieber, C. M. Tuning Light Absorption in Core/Shell Silicon Nanowire Photovoltaic Devices through Morphological Design Nano Lett. **2012**, 12 (9), 4971–4976.

(18) Ye, H.; Lu, P.; Yu, Z.; Song, Y.; Wang, D.; Wang, S. Critical Thickness and Radius for

Axial Heterostructure Nanowires Using Finite-Element Method Nano Lett. **2009**, 9 (5), 1921–1925.

(19) Glas, F. Critical Dimensions for the Plastic Relaxation of Strained Axial Heterostructures in Free-standing Nanowires Phys. Rev. B **2006**, 74 (121302), 1–4.

(20) Thelander, C.; Agarwal, P.; Brongersma, S.; Eymery, J.; Feiner, L. F.; Forchel, A.; Scheffler, M.; Riess, W.; Ohlsson, B. J.; Goesele, U.; Samuelson, L. Nanowire-based One-dimensional Electronics Mater. Today **2006**, 9 (10), 28–35.

(21) Gudiksen, M. S.; Lauhon, L. J.; Wang, J.; Smith, D. C.; Lieber, C. M. Growth of Nanowire Superlattice Structures for Nanoscale Photonics and Electronics Nature **2002**, 415 (February), 617–620.

(22) Lauhon, L. J.; Gudiksen, M. S.; Wang, D.; Lieber, C. M. Epitaxial Core–Shell and Core–Multishell Nanowire Heterostructures Nature **2002**, 420 (2001), 57–61.

(23) Borgstr, M. T.; Magnusson, M. H.; Dimroth, F.; Siefer, G.; Oliver, H.; Riel, H.; Member, S.; Schmid, H.; Wirths, S.; Bj, M.; Member, S.; Peijnenburg, W.; Vijver, M.; Tchernycheva, M.; Piazza, V. Towards Nanowire Tandem Junction Solar Cells on Silicon IEEE J. Photovoltaics **2018**, 8 (3), 733–740.

(24) Anttu, N.; Dagytė, V.; Zeng, X.; Otnes, G.; Borgström, M. Absorption and Transmission of Light in III–V Nanowire Arrays for Tandem Solar Cell Applications Nanotechnology **2017**, 28 (20), 205203.

(25) Ferrini, R.; Guizzetti, G.; Patrini, M.; Parisini, A.; Tarricone, L.; Valenti, B. Optical

Functions of InGaP/GaAs Epitaxial Layers from 0.01 to 5.5 eV Eur. Phys. J. B **2002**, 27 (4), 449–458.

(26) Özen, Y.; Akin, N.; Kinaci, B.; Özçelik, S. Performance Evaluation of a GaInP/GaAs Solar Cell Structure with the Integration of AlGaAs Tunnel Junction Sol. Energy Mater. Sol. Cells **2015**, 137, 1–5.

(27) Ishizaka, F.; Ikejiri, K.; Tomioka, K.; Fukui, T. Indium-Rich InGaP Nanowires Formed on InP (111)A Substrates by Selective-Area Metal Organic Vapor Phase Epitaxy Jpn. J. Appl. Phys. **2013**, 52 (111), 1–4.

(28) Berg, A.; Lenrick, F.; Vainorius, N.; Beech, J. P.; Wallenberg, L. R.; Borgström, M. T. Growth Parameter Design for Homogeneous Material Composition in Ternary GaxIn1−xP Nanowires Nanotechnology **2015**, 26 (435601), 1–8.

(29) Jacobsson, D.; Persson, J. M.; Kriegner, D.; Etzelstorfer, T.; Wallentin, J.; Wagner, J. B.; Stangl, J.; Samuelson, L.; Deppert, K.; Borgström, M. T. Particle-assisted GaxIn1−xP Nanowire Growth for Designed Bandgap Structures Nanotechnology **2012**, 235601 (24), 1–7.

(30) Svensson, C. P. T.; Mårtensson, T.; Trägårdh, J.; Larsson, C.; Rask, M.; Hessman, D.; Samuelson, L.; Ohlsson, J. Monolithic GaAs/InGaP Nanowire Light Emitting Diodes on Silicon Nanotechnology **2008**, 19 (305201), 1–6.

(31) Oliveira, D. S.; Tizei, L. H. G.; Li, A.; Vasconcelos, T. L.; Senna, C. A.; Archanjo, B. S.; Ugarte, D.; Cotta, M. A. Interaction Between Lamellar Twinning and Catalyst Dynamics in

Spontaneous Core–Shell InGaP Nanowires Nanoscale **2015**, 7 (29), 12722–12727.

(32) Kornienko, N.; Whitmore, D. D.; Yu, Y.; Leone, S. R.; Yang, P. Solution Phase Synthesis of Indium Gallium Phosphide Alloy Nanowires ACS Nano **2015**, 9 (4), 3951–3960.

(33) Algra, R. E.; Verheijen, M. A.; Borgström, M. T.; Feiner, L.-F.; Immink, G.; van Enckevort, W. J. P.; Vlieg, E.; Bakkers, E. P. A. M. Twinning Superlattices in Indium Phosphide Nanowires Nature **2008**, 456 (7220), 369–372.

(34) Otnes, G.; Heurlin, M.; Zeng, X.; Borgström, M. T. InxGa1−xP Nanowire Growth Dynamics Strongly Affected by Doping Using Diethylzinc Nano Lett. **2017**, 17 (2), 702–707.

(35) Haggren, T.; Kakko, J. P.; Jiang, H.; Dhaka, V.; Huhtio, T.; Lipsanen, H. Effects of Zn Doping on GaAs Nanowires 14th IEEE Int. Conf. Nanotechnology, IEEE-NANO 2014 **2014**, 825–829.

(36) Regolin, I.; Gutsche, C.; Lysov, A.; Blekker, K.; Li, Z. A.; Spasova, M.; Prost, W.; Tegude, F. J. Axial Pn-Junctions Formed by MOVPE using DEZn and TESn in Vapor–Liquid–Solid Grown GaAs Nanowires J. Cryst. Growth **2011**, 315 (1), 143–147.

(37) Gutsche, C.; Regolin, I.; Blekker, K.; Lysov, A.; Prost, W.; Tegude, F. J. Controllable -type Doping of GaAs Nanowires during Vapor-Liquid-Solid Growth J. Appl. Phys. **2009**, *105* (2), 024305, 1-5.

(38) Berg, A.; Caroff, P.; Shahid, N.; Lockrey, M. N.; Yuan, X.; Borgström, M. T.; Tan, H. H.; Jagadish, C. Growth and Optical Properties of InxGa1−xP Nanowires Synthesized by

Selective-area Epitaxy Nano Res. **2017**, 10 (2), 672–682.

(39) Schmid, H.; Borg, M.; Moselund, K.; Gignac, L.; Breslin, C. M.; Bruley, J.; Cutaia, D.; Riel, H. Template-assisted Selective Epitaxy of III–V Nanoscale Devices for Co-Planar Heterogeneous Integration with Si Appl. Phys. Lett. **2015**, 106 (23), 233101.

(40) Borg, M.; Schmid, H.; Moselund, K. E.; Cutaia, D.; Riel, H. Mechanisms of Template-Assisted Selective Epitaxy of InAs nanowires on Si J. Appl. Phys. **2015**, 117 (14), 144303.

(41) Knoedler, M.; Bologna, N.; Schmid, H.; Borg, M.; Moselund, K. E.; Wirths, S.; Rossell, M. D.; Riel, H. Observation of Twin-free GaAs Nanowire Growth Using Template- Assisted Selective Epitaxy Cryst. Growth Des. **2017**, 17 (12), 6297–6302.

(42) Borg, M.; Schmid, H.; Moselund, K. E.; Signorello, G.; Gignac, L.; Bruley, J.; Breslin, C.; Das Kanungo, P.; Werner, P.; Riel, H. Vertical III−V Nanowire Device Integration on Si(100) Nano Lett. **2014**, 14 (4), 1914–1920.

(43) Arroyo Rojas Dasilva, Y.; Kozak, R.; Erni, R.; Rossell, M. D. Structural Defects in Cubic Semiconductors Characterized by Aberration-Corrected Scanning Transmission Electron Microscopy Ultramicroscopy **2016**, 176, 11–22.

(44) Salehzadeh, O.; He, C.; Benyon, W.; SpringThorpe, A. J. The Effects of Zinc-Doping on the Composition of InGaAsP Layers Grown by MOCVD J. Cryst. Growth **2016**, 445, 110–114.

(45) Erni, R.; Browning, N. Valence Electron Energy-Loss Spectroscopy in Monochromated Scanning Transmission Electron Microscopy Ultramicroscopy **2005**, 104 (3–4), 176–192.

(46) Kong, X.; Albert, S.; Bengoechea-Encabo, A.; Sanchez-Garcia, M. a; Calleja, E.; Trampert, A.; Sanchez-García, M. A.; Calleja, E.; Trampert, A. Plasmon Excitation in Electron Energy-Loss Spectroscopy for Determination of Indium Concentration in (In,Ga)N/GaN Nanowires Nanotechnology **2012**, 23 (485701), 1–6.

(47) Auvergne, D.; Merle, P.; Mathieu, H. Band structure enhancement of indirect transitions Solid State Commun. **1977**, *21* (1), 437–439.

(48) Vurgaftman, I.; Meyer, J. R.; Ram-Mohan, L. R. Band parameters for III-V compound semiconductors and their alloys J. Appl. Phys. **2001**, *89* (11), 5815–5875.

(49) Dawson, M. D.; Duggan, G. Exciton Localization Effects and Heterojunction Band Offset in (Ga,In)P-(A1, Ga,In)P Multiple Quantum Wells Phys. Rev. B **1993**, 47 (19), 12598–12604.

(50) Ketterer, B.; Mikheev, E.; Uccelli, E.; Fontcuberta I Morral, A. Compensation mechanism in silicon-doped gallium arsenide nanowires Appl. Phys. Lett. **2010**, *97* (22), 1–4.

(51) Hetzl, M.; Kraut, M.; Winnerl, J.; Francaviglia, L.; Döblinger, M.; Matich, S.; Fontcuberta i Morral, A.; Stutzmann, M. Strain-Induced Band Gap Engineering in Selectively Grown GaN− (Al,Ga)N Core−Shell Nanowire Heterostructures Nano Lett. **2016**, 16 (11), 7098–7106.

(52) Su, L. C.; Pu, S. T.; Stringfellow, G. B.; Christen, J.; Selber, H.; Bimberg, D. Control of Ordering in GalnP and Effect on Bandgap Energy J. Electron. Mater. **1994**, 23 (2), 125–133.

(53) Wallentin, J.; Ek, M.; Wallenberg, L. R.; Samuelson, L.; Deppert, K.; Borgström, M. T. Changes in Contact Angle of Seed Particle Correlated with Increased Zincblende Formation in Doped InP Nanowires Nano Lett. **2010**, 10 (12), 4807–4812.

(54) Lin, J.; Wu, M.; Jou, M.; Chang, C.; Chen, C.; Lee, B. Growth and Characterization of Ga0.65In0.35P Orange Light-Emitting Diodes by Metalorganic Vapor–Phase Epitaxy J. Appl. Phys. **1993**, 74 (3), 1781–1786.

(55) Hÿtch, M. J.; Snoeck, E.; Kilaas, R. Quantitative Measurement of Displacement and Strain Fields from HREM Micrographs Ultramicroscopy **1998**, 74 (3), 131–146.

Table of Contents Graphic